Journal of Power Sources 192 (2009) 247–257

Contents lists available at ScienceDirect

Journal of Power Sources

journal homepage: www.elsevier.com/locate/jpowsour

$Ce_{0.9}Sr_{0.1}VO_x$ ($x = 3, 4$) as anode materials for H_2S-containing CH_4 fueled solid oxide fuel cells

Nemanja Danilovic, Jing-Li Luo*, Karl T. Chuang, Alan R. Sanger

Department of Chemical and Materials Engineering, University of Alberta, Alberta, Canada T6G 2G6

ARTICLE INFO

Article history:
Received 11 February 2009
Received in revised form 24 March 2009
Accepted 25 March 2009
Available online 2 April 2009

Keywords:
Solid oxide fuel cell
Hydrogen sulfide
Methane
Anode catalyst
Ce- and V-containing perovskite

ABSTRACT

The stability and activity in 0.5% H_2S–CH_4 of $Ce_{0.9}Sr_{0.1}VO_3$ and $Ce_{0.9}Sr_{0.1}VO_4$ anode materials for H_2S-containing CH_4 fueled SOFCs have been determined. XRD showed that $Ce_{0.9}Sr_{0.1}VO_4$ was reduced when the fuel gas was 0.5% H_2S–CH_4, while $Ce_{0.9}Sr_{0.1}VO_3$ remained stable over 24 h at 950 °C. Electrochemical tests in 0.5% H_2S–CH_4 showed stable performance at 950 and 800 °C for cells comprising $Ce_{0.9}Sr_{0.1}VO_3$|YSZ|Pt. Comparison of fuel cell performances using 0.5% H_2S–CH_4, 0.5% H_2S–N_2 and 5% H_2S–N_2 as feeds showed that $Ce_{0.9}Sr_{0.1}VO_3$ was not active for oxidation of methane, but highly active for conversion of H_2S. Electrochemical impedance results were consistent with the finding that the anode was activated only in an environment that contained H_2S. Conductivity measurements showed there was an increase in conductivity in H_2S-containing environments, and that this increase resulted from a change in composition and structure from the oxide to monoclinic $Ce_{0.9}Sr_{0.1}V(O,S)_3$, as evidenced by XPS and XRD analyses.

1. Introduction

Fuel cells are electrochemical devices that efficiently convert chemical energy of a fuel to electrical energy. Solid oxide fuel cells (SOFCs) are high temperature fuel cells in which the solid electrolyte is an oxide ion conducting membrane. SOFCs are suitable for many stationary power generation and back-up power applications. SOFCs can be fueled using a variety of fuels, including hydrogen, methane (both directly and with reformed methane), ethanol, and syngas (coal gas) [1–8]. While H_2S is recognized as a problem in operating conventional SOFC as it can poison typical catalysts and is corrosive, it also has been recognized that there is potential utility in using as fuel feeds which contain H_2S, and in some cases there is benefit in terms of performance [9–18].

H_2S is a poisonous gas which is a common constituent of oil and gas deposits and is produced as a by-product of refining. Natural gas which contains at least 50 ppm of H_2S is termed "sour" natural gas, of which a typical composition is shown in Table 1 [19,20]. Sour natural gas must be "sweetened" before transportation and use, due to the dangerous and corrosive nature of H_2S. Further H_2S removal is required before use of natural gas as a fuel in SOFCs in order to lower the H_2S content below 5 ppm to minimize damage to and degradation of performance of Ni–YSZ anodes [7–15,21–24]. A SOFC with H_2S tolerance is highly desirable because it would not require a similar amount of fuel preconditioning, leading to decreased peripheral systems requirements, hence lower operating and capital costs. Furthermore, if an SOFC can handle H_2S content from 500 ppm up to several vol.%, it would be able to utilize sour natural gas directly. An alternative benefit of SOFCs capable of converting H_2S but not hydrocarbons is that they could be used to sweeten sour natural gas while co-generating power.

Mixed metal oxides have emerged in the last 10 years as interesting candidate anode materials for SOFCs with good electronic and ionic conductivity at elevated temperatures, stability against carbon deposition and sulfur poisoning, and good catalytic activity for oxidation of hydrocarbon fuels [25,26]. In this study we showed the potential utility of new Ce- and V-containing oxide materials having perovskite (ABO_3) or zircon (ABO_4) types of structure [25,27,28].

V^{n+} ($n = 3, 5$ for perovskite and zircon types of structure, respectively) was selected as the B-site cation as it has been shown that vanadium has promising catalytic activity for conversion of a variety of fuels in fuel cells [29–33]. A power density of 275 mW cm^{-2} was achieved using $La_{0.7}Sr_{0.3}VO_3$ for conversion of 5% H_2S–CH_4 at 950 °C [29]. Consequently, to evaluate the role of the A-site cation, Ce^{3+} was selected as the A-site cation in both the perovskite and zircon-type anodes as it was expected to confer catalytic activity and redox stability, whereas La^{3+} typically was used in prior investigations utilizing perovskite catalysts [29,33]. However, it was recognized that the different valence states available for $Ce^{3+/4+}$ can provide a secondary active site on the surface of the anode, and a recent patent lists several Ce based perovskites as anodes for SOFCs [34]. The combination of Ce and V in an anode catalyst is precedented:unpromoted $CeVO_3$ and $CeVO_4$ each showed

* Corresponding author. Tel.: +1 780 492 2232; fax: +1 780 492 2881.
E-mail address: Jingli.Luo@ualberta.ca (J.-L. Luo).

0378-7753/$ – see front matter © 2009 Elsevier B.V. All rights reserved.
doi:10.1016/j.jpowsour.2009.03.045

Table 1
Typical composition of sour natural gas [19,20].

Component	vol.%
Methane	85
Ethane	6
Propane	2
Nitrogen	3
Carbon dioxide	1
Higher hydrocarbons	1
Hydrogen sulfide	>4 ppm

significant activity when tested as oxidation catalysts for H_2S and hydrocarbon fuels at intermediate temperatures [35–37].

2. Experimental

2.1. Catalyst preparation

$Ce_{0.9}Sr_{0.1}VO_3$ (CSV3) and $Ce_{0.9}Sr_{0.1}VO_4$ (CSV4) were prepared by solid state synthesis from the powdered oxide precursors: SrO_2 (Alfa Aeser), CeO_2 (Sigma–Aldrich, 99.9%) and V_2O_5 (Alfa Aeser, 98%). The powders were mixed in a ball mill for 24 h, then sintered in alumina boats at 1100 °C in 10% H_2–Ar (CSV3) and N_2 (CSV4) for 6 h. This procedure was repeated until the desired phase was formed as the single or predominant material, as shown by XRD analysis (Fig. 2).

2.2. Fuel cell testing

Membranes were prepared by painting platinum paste (Heraeus, 1 cm^2) onto YSZ (8 mol% Y_2O_3, Intertec Southwest, 25.4 mm OD, 0.3 mm thick) onto the electrolyte to form the cathode, and calcining at 900 °C in air for 1 h. The anode catalyst, either CSV3 or CSV4, was ground using a mortar and pestle and dispersed in α-terpineol to form a paste, and a 1 cm^2 area was screen printed onto the opposite face of the electrolyte to form a membrane electrode assembly (MEA). The MEA was presintered in 10% H_2–Ar for 2 h at 1000 °C. Typical anode thicknesses were about 50 μm, while the cathode thicknesses were 5–10 μm.

The MEA was installed in the fuel cell testing apparatus as shown schematically in Fig. 1. Gold current collector wires (single probe) with spiral wound ends ran through the length of the inlet tube. During a typical MEA installation, ceramic sealant (Aremco, Type 503) was applied to an end of the outlet anode tube, and the MEA was placed onto the sealant. The sealant was then cured, using the procedure prescribed by Aremco, while the cell was heated at 2 °C min^{-1} to a prescribed operating temperature, in flowing 1% H_2-N_2 gas. The flow rates of operating fuel cell gas feeds (i.e. air on cathode side and fuel on anode side) then were set using flow controllers (Arbin Instruments Solid Oxide Fuel Cell Test Station, MKS mass flow controllers); flow rates used at each of the anode and cathode sides were 200 cm^3 min^{-1} in all comparative tests. The chamber volume was close to 80 cm^3; LHSV 150 h^{-1}. Fuel cell testing was conducted with standard DC and AC electrochemical techniques using a Solartron 1287A Potentiostat/Galvanostat (5 mV s^{-1} sweep rate was used for potentiodynamic tests) and a Solartron 1252A FRA (electrochemical impedance was analyzed from 1 MHz to 0.5 Hz, at OCV and ±20 mV). Fuel cell tests were conducted using a two electrode setup. The wire resistance was manually compensated by externally measuring the wire resistance at testing temperature.

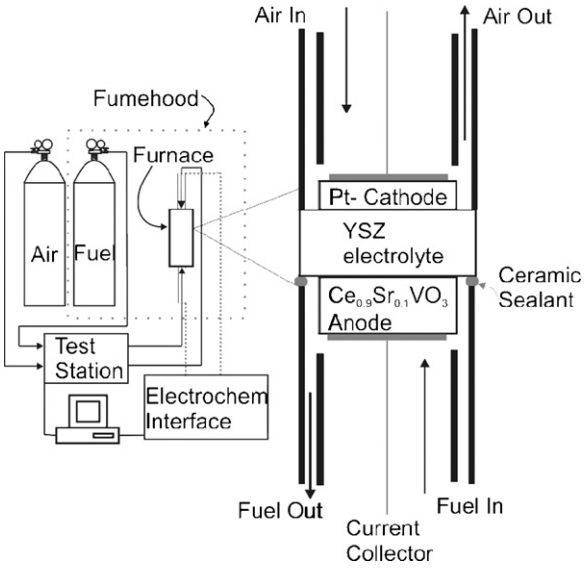

Fig. 1. Schematic of fuel cell setup.

2.3. Conductivity testing

Conductivity measurements were conducted in a commercial NorECs Probostat electrochemical measurement cell using gold mesh current collectors (two probes) in a single gas environment. Cylindrical pellets were prepared by pressing powdered catalyst at 2 tonnes in a 1 cm ID die, and the pellet so formed was fired at 1250 °C in 1% H_2–N_2 for 2 h. Gold paste was painted on both sides of the pellet and fired at 800 °C in 1% H_2–N_2 for 1 h. The combinations of gases used during the tests were 10% H_2–N_2 and 5% H_2S–N_2, each flowing at 50 mL min^{-1}. The samples were heated at 2 °C min^{-1} and tests were performed at selected temperatures in the range 500–950 °C. Measurements were made using the two point DC conductivity method and the samples were held at each testing temperature until stable conductivity was achieved. Typically, in H_2 atmospheres stable values were obtained 2 h after stabilization of the testing temperature. Under an H_2S-containing environment the sample typically was held at 925 °C for 24 h before a constant conductivity was achieved, whereas at lower temperatures stable conductivity values were achieved within 2 h.

2.4. Chemical stability testing

Chemical stability tests were conducted using powdered samples of anode materials in an alumina boat. The samples were heated in a stream of flowing N_2, held at 1000 °C in 0.5% H_2S–CH_4 (Praxair) for 12 h, and then cooled, again in a stream of flowing N_2. Chemical stability was also determined for samples that had been used for conductivity testing. The phase composition of the powders was determined using XRD.

2.5. Materials characterization

A Rigaku RU200 Powder X-ray diffraction (XRD) system with a rotating anode and a Co target was used for analysis of all synthesized powders, with a scan rate of 2° θ min^{-1}. The commercially available software Jade® was used for identifying phases present in the samples.

A Hitachi S-4800 field emission scanning electron microscope (SEM) was used for characterizing cross-sections of MEAs.

X-ray photoelectron spectroscopy (XPS) was performed on samples using a Kratos Analytical AXIS 165. A monochromated Al Kα ($h\nu$ = 1486.6 eV) source was used at a power of 210 W, with a base pressure of 3×10^{-8} Pa in the analytical chamber. Fixed analyzer transmission (FAT) mode was applied with a resolution of 0.55 eV for Ag 3d and 0.70 eV for Au 4f peaks. The analysis spot was 700 μm × 300 μm. Charge neutralization (current 1.7 A, balance

1.8 V, bias 1.1 V) was applied to compensate for photoelectrons leaving the sample surface. After degassing, survey scans between 1100 and 0 eV were collected at a pass energy of 160 eV, 0.35 eV step size and a dwell time of 200 ms, and were accumulated over three scans. Narrow scans of Ce, V, O and S were collected at 20 eV pass energy, 0.1 eV step size and 200 ms dwell time and 10–20 scans per sample. Spectra were referenced to C 1s binding energy of 283.26 eV, and were fitted using Gaussian–Lorentzian peak shapes and Shirley baselines.

Differential scanning calorimetry–thermogravimetric analysis (DSC-TGA) was performed using a TA Instruments SDT Q600. Precisely measured powder samples weighing about 20 mg were placed in an alumina cup (90 μL) under a flowing stream comprising 100 mL min^{-1} N_2 and 1 mL min^{-1} H_2. The sample was heated at 20 °C min^{-1} to 850 °C and held for 30 min until the signal stabilized, then the stream to the chamber was switched to 200 mL min^{-1} of 500 ppm H_2S (in N_2) at a constant temperature for 20 min. The sample was subsequently cooled under N_2.

Quantachrome Instruments Autosorb I was used for BET surface area determinations of the freshly prepared reduced catalysts.

3. Results

3.1. Characterization of anode materials

The XRD pattern of as-prepared CSV3 (PDF# 25-0307) showed that it possessed a perovskite structure with a tetragonal unit cell and lattice parameters $a = 5.52$ Å and $c = 7.81$ Å (Fig. 2a). To form this structure Ce must be present in the 3+ oxidation state, and V predominantly as 3+; the substituent Sr is 2+. Analysis of the XRD pattern of CSV4 (PDF# 12-0757) (Fig. 2b) showed a zircon-type tetragonal unit cell, with lattice parameters $a = 7.36$ Å and $c = 6.49$ Å. For this structure Ce must be in the 3+ oxidation state, V predominantly as 5+; again, substituent Sr is 2+.

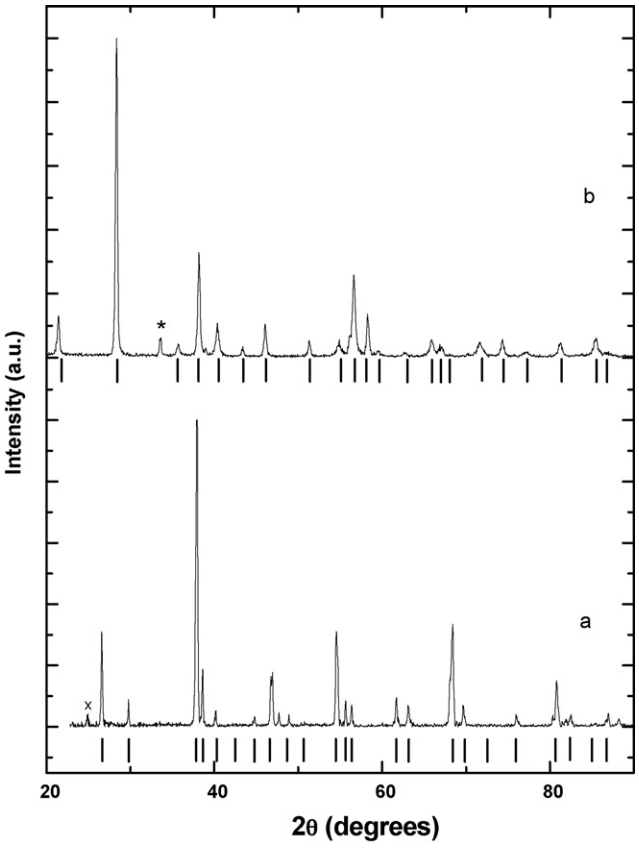

Fig. 2. XRD patterns of fresh (a) $Ce_{0.9}Sr_{0.1}VO_3$ and (b) $Ce_{0.9}Sr_{0.1}VO_4$.

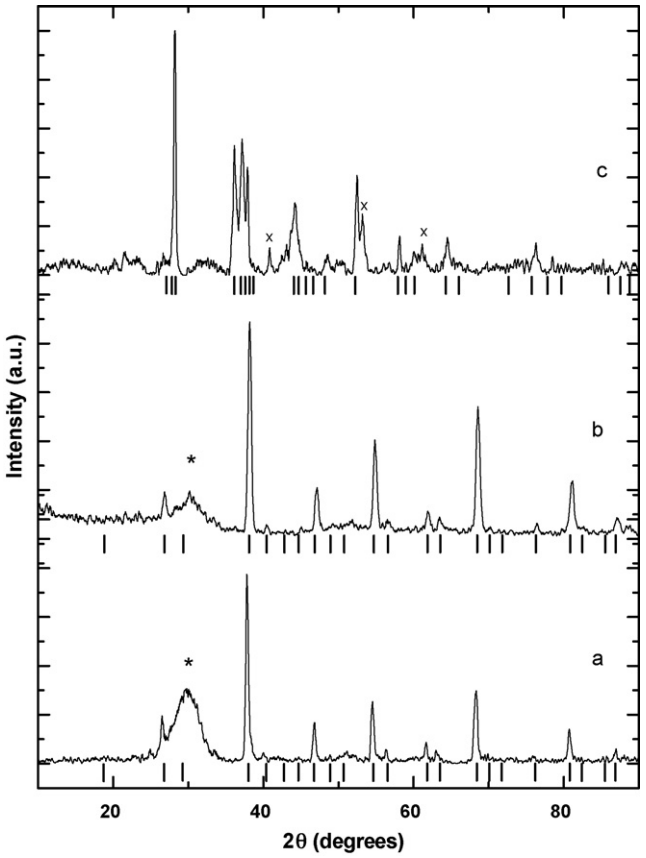

Fig. 3. XRD patterns of (a) $Ce_{0.9}Sr_{0.1}VO_3$ after stability test, (b) $Ce_{0.9}Sr_{0.1}VO_4$ after stability test and (c) sulfided $Ce_{0.9}Sr_{0.1}VO_3$ formed after conductivity test. (*Indicates amorphous carbon.).

The BET surface areas of fresh catalyst materials were low, 1.17 m^2 g^{-1} (CSV3) and 2.38 m^2 g^{-1} (CSV4).

3.2. Chemical stability of anode materials

XRD analyses conducted after the chemical stability tests of $Ce_{0.9}Sr_{0.1}VO_3$ in 0.5% H_2S–CH_4 showed that the used material retained the structure of fresh material (Fig. 3a), and that no discernable amounts of sulfur-containing phases were present. Thus there was no reaction or decomposition of the oxide. However, there was a larger amorphous background between 25° and 35° 2θ which was ascribed to carbon present in the powder that had been formed by thermal cracking of methane at 1000 °C.

CSV4 was reduced in the gas mixture, and the XRD pattern of the tested sample matched that of CSV3 (Fig. 3b). Again, there were no sulfur-containing phases present, and the only change was the presence of a stronger background signal of carbon between 25° and 35° 2θ. In this case it appeared that the carbon included material formed by methane decomposition that flaked from the walls of the quartz tube onto the sample during retrieval.

Separate MEAs with CSV4 and CSV3 as anodes screen-printed onto the electrolyte were presintered at 1000 °C prior to testing. CSV4 was reduced during the presintering of the MEA in 10% H_2–Ar which, due to a dimensional change of the anode relative to YSZ, led to delamination of the anode from the electrolyte, with consequent high resistance and no useful activity for activation of the fuel. Sintering CSV4 in N_2 and testing under reducing conditions also led

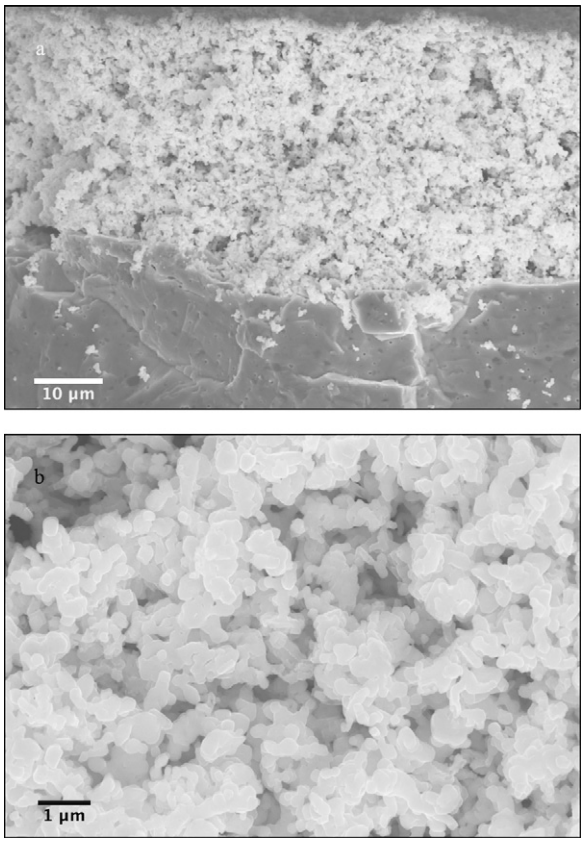

Fig. 4. SEM image of (a) cross-section of prepared MEA and (b) higher magnification of $Ce_{0.9}Sr_{0.1}VO_3$ anode.

to rapid delamination of the anode arising from reduction of the oxide.

In contrast, CSV3 formed a stable bond with the surface of YSZ and, as a result, adhered well to the electrolyte throughout tests. Fig. 4 shows a cross-sectional SEM image of a CSV3|YSZ|Pt MEA. It was found that CSV3 was stable under a reducing atmosphere, as the performance of MEAs remained high and stable as long as the cells remained hot. The material was prone to cracking during cool down. Such cracking may have occurred as a result of differential thermal expansion or contraction between components. However, in the present case we found it most unlikely that there was differential expansion. The interface was stable throughout presintering and testing. During the presintering process there was good adhesion between the pure anode CSV layer and the YSZ electrolyte, even without roughening the surface of the YSZ. Further, during fuel cell testing, in which the anode was exposed to H_2S and a sulfidation reaction occurred, there was no loss in power density, showing that there was no delamination at that time. Thus there was a stable interface between either the unsulfided anode or the sulfide anode and the electrolyte. It was found that delamination occurred only during cool down, during which it was found that the sealant tended to crack. Thus, while we cannot unequivocally state that there was no differential contraction during cool down, we attributed the cracking to consequences of sealant cracking, possible resulting in oxidation of the anode material.

3.3. Electrochemical performance

Potentiodynamic tests were conducted to determine the electrochemical activity of the anode material for conversion of each of methane and H_2S. The MEAs were tested at 950 and 800 °C, in separate tests for each of the feeds 0.5% H_2S–CH_4 (to simulate

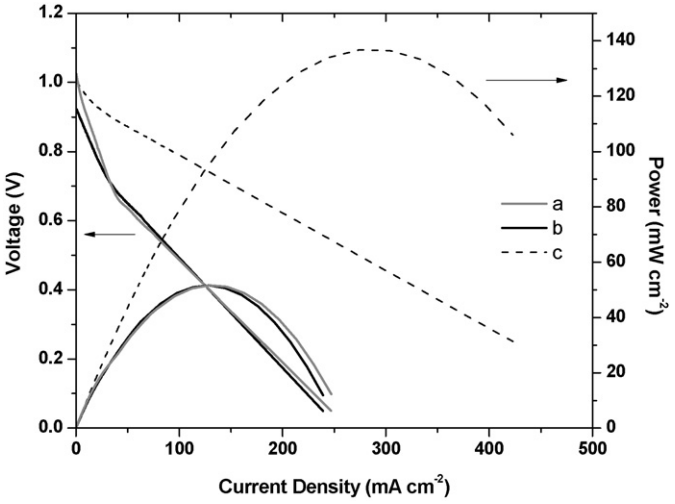

Fig. 5. Potentiodynamic curves for sulfided $Ce_{0.9}Sr_{0.1}VO_3$|YSZ|Pt at 950 °C in (a) 0.5% H_2S–CH_4, (b) 0.5% H_2S–N_2 and (c) 5% H_2S–N_2.

sour gas), 0.5% H_2S–N_2, 5% H_2S–N_2, and pure CH_4. The initial tests were performed using sour gas, but it was necessary to ascertain if one or both components of the gas contributed to the activity of the cell, hence we also used H_2S with balance N_2 and pure CH_4 in comparative tests (Figs. 5 and 6). The performances were similar for both 0.5% H_2S–CH_4 and 0.5% H_2S–N_2 at 950 °C, but a slight difference was found at 800 °C, where use of the 0.5% H_2S–N_2 feed provided a slightly higher power output by about 5 mW cm^{-2}. When the concentration of H_2S was increased to 5%, the performance increased to a maximum power density of 140 mW cm^{-2} (950 °C) and 120 mW cm^{-2} (800 °C). These values are high for a feed having such a low concentration of H_2S, and so show the high activity of the sulfided anode catalyst for conversion of H_2S [9–15].

Fig. 7 shows the impedance spectra for the MEA having the same CSV3 anode at 950 °C in different gas mixtures. The impedance arising from diffusion of H_2S to the active sites increased with decreasing H_2S content due to dilution. The high frequency intercept, R_S, did not change significantly between the spectra when using different fuels, and the value for R_{P1} (combined cathode and electrolyte resistance) was also similar in each case. In contrast, the value for R_{P2} (anode resistance) increased 2-fold when using 0.5%

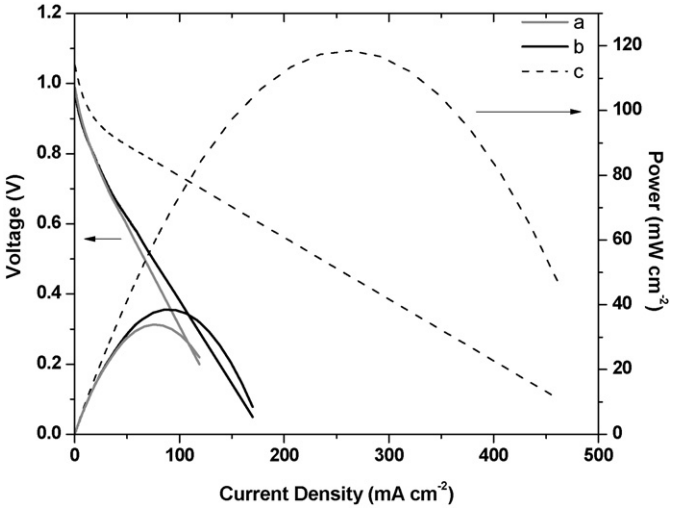

Fig. 6. Potentiodynamic curves for sulfided $Ce_{0.9}Sr_{0.1}VO_3$|YSZ|Pt at 800 °C in (a) 0.5% H_2S–CH_4, (b) 0.5% H_2S–N_2 and (c) 5% H_2S–N_2.

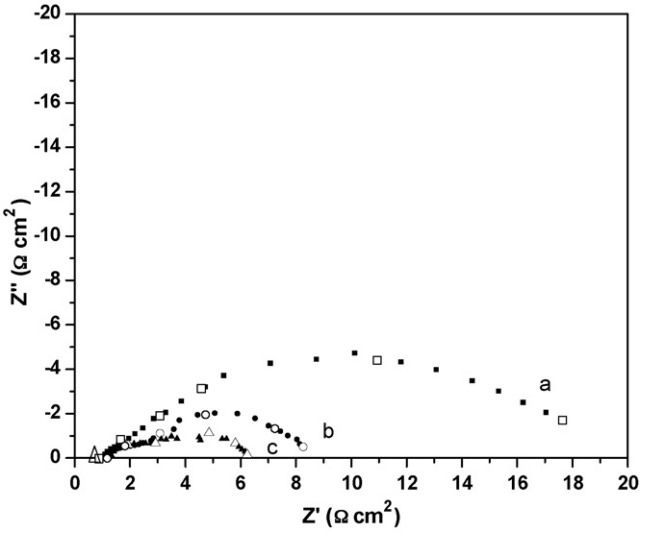

Fig. 7. Impedance spectra of sulfided $Ce_{0.9}Sr_{0.1}VO_3$|YSZ|Pt at 950 °C in (a) 0.5% H_2S–CH_4, (b) 0.5% H_2S–N_2 and (c) 5% H_2S–N_2. (Frequency decades 1×10^5 to 1×10^{-1} are labelled.).

Table 2
Summary of impedance results at 950 °C (Ω cm²).

	0.5% H_2S–N_2	0.5% H_2S–CH_4	5% H_2S–N_2
R_S	1.247	1.035	1.296
R_{P1}	1.16	1.031	1.261
R_{P2}	4.8	10.7	1.93
R_{P3}	N/A	N/A	2.17

H_2S–CH_4 and 0.5% H_2S–N_2. The data are summarized in Table 2. Fig. 8 shows the stability of the catalyst in 0.5% H_2S–CH_4 over a 2.5 h period at 80 mA cm^{-2}. There was no degradation of the voltage after an initial decrease, ascribed to conditioning of the catalyst, and there was no detectable carbon deposition on the anode as determined by analysis after cooling to room temperature. If, however, there was an undetected negligible amount of carbon deposited as a result of thermal processes, the amount was so small that it could not be seen either visually or using SEM, and there was no effect on electrochemical performance as there was no increase in overpotential during the galvanostatic tests. However, under more strenuous conditions these and similar catalysts are prone to coking [38].

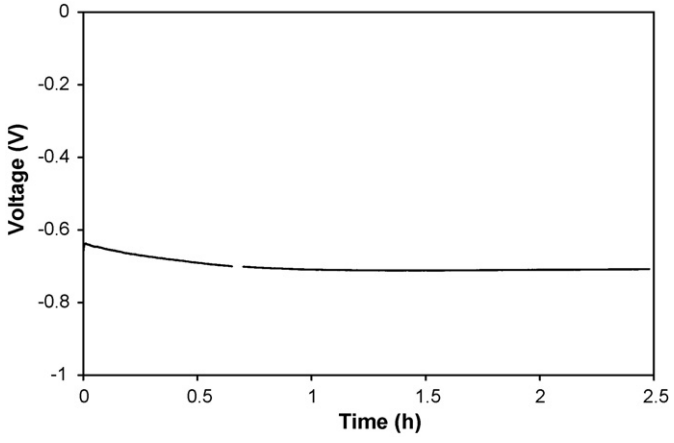

Fig. 8. Long term galvanostatic test of sulfided $Ce_{0.9}Sr_{0.1}VO_3$|YSZ|Pt in 0.5% H_2S–CH_4 at 950 °C and 40 mA cm^{-2}.

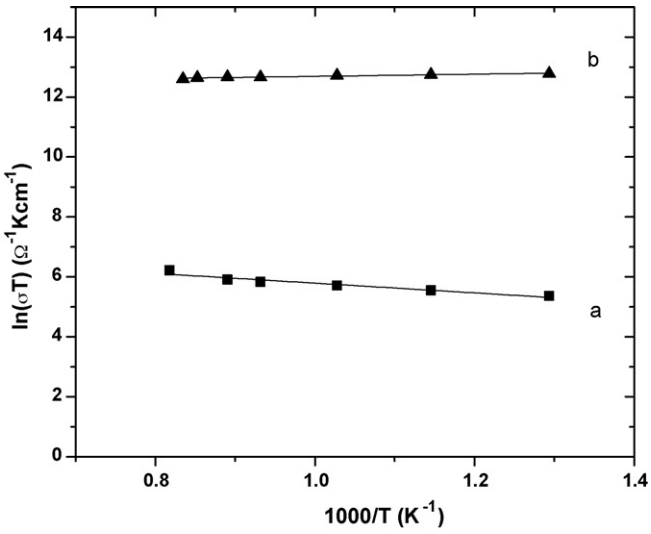

Fig. 9. Conductivity of $Ce_{0.9}Sr_{0.1}VO_3$ in (a) 10% H_2–N_2 and (b) sulfided catalyst in 5% H_2S–N_2.

3.4. Total conductivity

The total conductivity of CSV3 was determined under a range of conditions to determine the effects of atmosphere and temperature on its electrochemical properties. The conductivity of CSV3 in H_2 increased with increasing temperature (Fig. 9a), behaviour typical of semiconductors and ionic conductors [39]. The activation energy was 0.106 eV. The conductivity of the same material in H_2S (Fig. 9b) decreased with increasing temperature, which behaviour is typical of metallic and pseudo-metallic conductors. The conductivity at 925 °C increased greatly from a value of 0.41 S cm^{-1} in the H_2-containing environment to 248 S cm^{-1} in the corresponding H_2S-containing environment. The activation energy of conduction in the H_2S-containing environment was −0.120 eV, indicating that the conductivity of the anode was pseudo-metallic in character.

XRD and XPS analyses were conducted on both fresh and used pellets to determine whether the change in conductivity was associated with changes in the composition or structure of the material, which were not evident visually. The gold electrode paste was removed, and the pellet was ground to a fine powder. XRD analysis of the powder showed that the material had undergone a chemical reaction with H_2S, to form a material having a structure similar to that of fully sulfided $Ce_{0.9}Sr_{0.1}VS_3$. However, the XRD pattern was not fully consistent with that of $Ce_{0.9}Sr_{0.1}VS_3$, as seen by comparing the peak positions and intensities with that of the sulfide (PDF# 47-1039) (Fig. 3c).

3.5. Thermal analysis

In order to gain more insight into the reaction that occurred between H_2S and CSV3, the material was exposed to H_2S while under a H_2 atmosphere at 850 °C in a DSC/TGA instrument. The weight and heat flow changes were monitored using TGA and DSC, respectively (Fig. 10a and b). The signal was allowed to stabilize for ~30 min upon reaching the reaction temperature as some further reduction reaction was occurring to the already reduced sample.

There was an initial increase in weight and an exothermic heat flow. The weight gain was 0.07805 mg which, assuming that it is totally ascribable to adsorbed H_2S, constitutes 2.61×10^{18} molecules (4.34×10^{-6} mol). Assuming that chemisorbed H_2S dissociated to form a monolayer of adsorbed S atoms, and if the catalyst particle geometry was approximated as spherical, this constituted

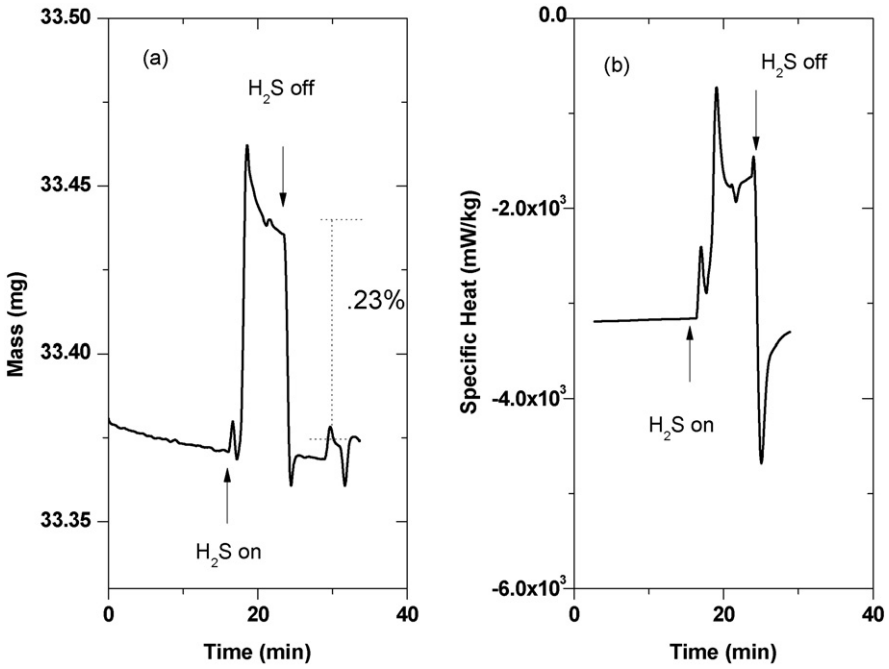

Fig. 10. Effect on the (a) mass (TGA) and (b) specific heat (DSC) on exposure of CSV3 at 850 °C to 5000 ppm of H_2S in H_2. (A rising value indicated exothermicity in the DSC.).

about 15% partial surface coverage. The DSC signal also showed an exothermic peak followed by an increased heat capacity, which was indicative of adsorption and a change in the phase of the material. After 15 min the H_2S flow was stopped and pure H_2 continued to flow, which was followed, starting essentially immediately, by a gradual return to the original weight as the adsorbed S was desorbed as it reacted with H_2 to reform H_2S. In addition, trace amounts of SO_2 were also detected in the effluent, attributed to continuing reaction of sulfur with oxygen anions to form SO_2 and regenerate electrons. Since the DSC/TGA instrument used horizontal beams to position the samples in the reactive gas flow, buoyancy effects were minimized. Blank trials using empty alumina cups did not show the same response as those shown in Fig. 9, signifying that the reaction measured was adsorption of H_2S onto the catalyst sample.

3.6. XPS analyses

XPS was employed to determine the near-surface composition and near-surface ion electronic states of fresh $Ce_{0.9}Sr_{0.1}VO_3$ and the sulfided material, either $Ce_{0.9}Sr_{0.1}VS_3$ or $Ce_{0.9}Sr_{0.1}V(S,O)_3$, formed during conductivity measurements in 5% H_2S atmosphere. Fig. 11 shows high resolution sweeps of the main ionic components in the two materials. The compositions and peak locations are summarized in Table 3.

Ce had five peaks attributed to $d^{5/2}$ and $d^{3/2}$ orbitals in the fresh sample while there were only four peaks in the spectrum of the sulfided material. The highest energy peak for Ce, at 914.78 eV, was not present after sulfidation. Two peaks at 883.92 and 898.03 eV were shifted by about 0.5 eV to higher energies after sulfidation. The increase in binding energy may be related to an increase in oxidation state of a portion of Ce from Ce^{3+} to Ce^{4+} with sulfidation, since a more electropositive bond with S would decrease the binding energy. However, we will show below that the ratio of surface total anions/cations did not change by more than a small fraction, and so any partial change in oxidation state was small. Therefore it may be that the change in peak position was attributable to a change in the anion bonded to the Ce cations.

Bond energy shifts of the V peaks were also detected following sulfidation, as the lowest energy $2p^{3/2}$ peak at 515.35 eV shifted by 1 eV to a lower energy while the higher energy peak stayed at the same energy of 515.6 eV. After sulfidation the two $2p^{1/2}$ peaks appeared to merge into one peak, the value of which was centered between those of the original peaks. The decrease in binding energy of some peaks signified predominantly V–S bonding as opposed to V–O bonding.

The lower energy O peak did not shift in energy, 528.4 eV, but the higher energy peak at 529.63 eV increased by about 0.5 eV. The relative areas of the two peaks (528.3/529.6 eV) also changed with sulfidation from 60/40 to 40/60, evidence that there were two different bonding states present for oxygen and, as shown below for sulfur as well [40–42], the first being a structural O^{2-}, while the second being a bridging oxygen.

The spectrum for sulfur showed two pairs of overlapping peaks. The lower energy peak was attributed to a structural sulfur, S^{2-}, while the higher energy peak was attributed to a bridging sulfur.

Thus there is a change in the composition of the surface which may have been, for example, from M–O–M(O)–O–M to M–O–M(S)–O–M, or from M–O–M(O)–O–M to M–S–M(O)–O–M either of which would change the ratio of surface O to bridging O, where M indicates a cation, –O– and –S– indicate bridging anions, while (O) and (S) indicate terminal O and S.

The oxygen to metal cation ratio (O/cat) at the surface of fresh CSV3 was 2.3, whereas the sulfided CSV3 had an O/cat ratio of 1.9 and a sulfur to cation ration (S/cat) of 0.43. Thus the formulation of the sulfided materials is best represented by the formula $Ce_{0.9}Sr_{0.1}V(S,O)_3$, and the ratio of O/S was 4.5 and the surface (O + S)/cat ratio was 2.3. Hence the ratio of total surface anions/cations was in each case close to 2.3.

4. Discussion

Due to the instability of CSV4 under reducing conditions, as shown by the changes to the XRD spectra of the material under methane, leading to a phase change and concomitant large dimensional change, this material is not a suitable anode catalyst.

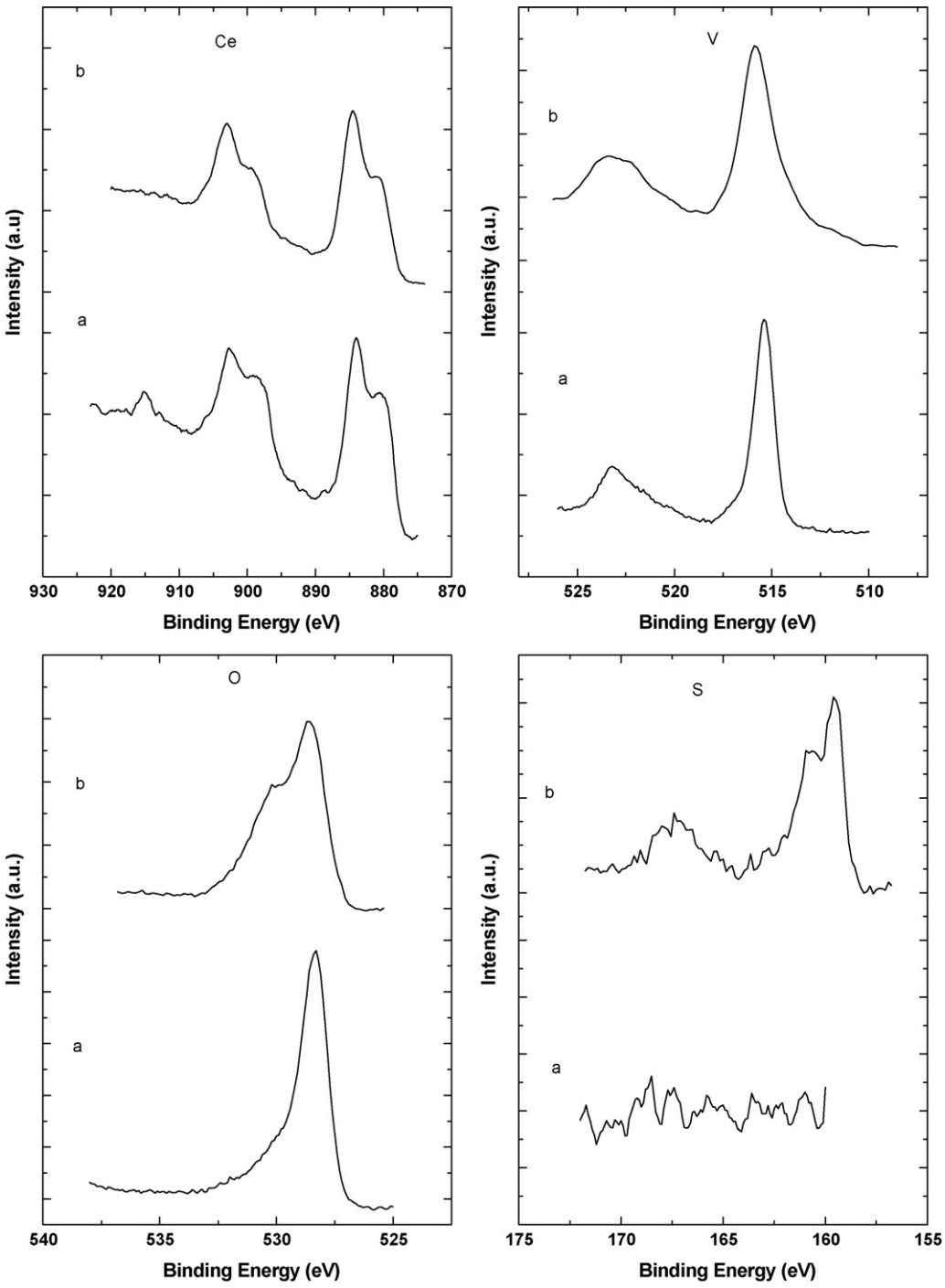

Fig. 11. XPS spectra for different elements of (a) fresh and (b) sulfided $Ce_{0.9}Sr_{0.1}VO_3$.

Thermodynamic analysis showed that $CeVO_4$ was not stable at low oxygen partial pressures and higher temperatures, as summarized in Fig. 12. Thermochemical data for this analysis were obtained from Ref. [43] and the analysis was conducted according to the procedure developed by Yokokawa et al. [44]. Hence, assuming non-doped structures of $CeVO_3$ and $CeVO_4$, the reduction of the anode reaction (1) under reducing atmospheres (0.5% H_2S–CH_4 or 10% H_2–N_2) was to be expected.

$$CeVO_4 \rightarrow CeVO_3 + (1/2)O_2 \quad (1)$$

$$\Delta G_{rxn} = \Delta G_f(CeVO_3) + (1/2)\Delta G_f(O_2) - \Delta G_f(CeVO_4) \quad (2)$$

The plot of dependence of partial pressure of oxygen on temperature, Fig. 12, is derived from reactions (1) and (2). Because $CeVO_4$ readily undergoes reduction by loss of oxygen, the primary focus in this work was on structural and electrochemical characterization of CSV3.

The XRD of anode samples CSV3 (Fig. 3a) that were treated in the fuel gas atmosphere showed that there were no changes to the bulk crystal structure. However, a strong background signal was clearly evident, due to carbon deposited on the entire quartz tube as a result of CH_4 decomposition during the test which then flaked off onto the sample during extraction. It is interesting that these findings differed from the XRD pattern of the tested material after conductivity measurements (Fig. 3c) which

Table 3
Summary of XPS data.

	Ce					V				O		S		
	$3d^{5/2}$	$3d^{5/2}$	$3d^{3/2}$	$3d^{3/2}$	$3d^{3/2}$	$2p^{3/2}$	$2p^{3/2}$	$2p^{1/2}$	$2p^{1/2}$	1s	1s	2p	2p	2p
CSV														
Area	5895	7868	5592	5382	1048	2299	1364	917	627	5517	3371			
FWHM	3.23	3.49	4.44	4.43	3.08	1.04	2.16	2.82	1.44	1.19	2.68			
Position	880.00	883.93	898.03	902.50	914. 78	515.35	515.74	521.82	523.23	528.32	529.63			
Concentration (%)	22.76	30.43	21.74	20.97	4.10	44.17	26.19	17.60	12.03	62.08	37.92			
CSV-S														
Area	4531	6760	2089	4846		1577	1956	1365		3395	4433	376.90	352.10	196.60	329.8
FWHM	3.52	3.40	2.98	4.08		3.49	1.52	3.10		1.34	2.44	0.94	1.34	2.74	2.75136
Position	880.30	884.25	898.57	902.63		514.37	515.60	522.58		528.45	530.04	159.48	160.68	162.04	167.21
Concentration (%)	24.77	37.01	11.60	26.72		32.20	39.93	27.87		43.37	56.63	20.36	28.37	15.66	26.21

showed the formation of $Ce_{0.9}Sr_{0.1}V(O,S)_3$. This result is most likely due to the difference in concentration of H_2S, which was 10 times greater in the conductivity measurement case, as well as the lower oxygen partial pressure in the conductivity setup. The susceptibility of the material to sulfidation and the degree of sulfidation appeared to be a function of the amount of H_2S under conductivity conditions, since during the chemical stability test the material did not appear to be sulfided to any significant degree. This suggests very fast oxygen–sulfur ionic exchange kinetics under polarization conditions. The DSC/TGA data (Fig. 10) showed that saturation of adsorbed H_2S species happened very rapidly at 850 °C.

It is noteworthy that sulfidation was not accompanied by any significant redox reaction. The ratio of total surface anions/cations in each of the unsulfided and sulfided materials was close to 2.3, indicating that the primary reaction on sulfidation was replacement of O^{2-} by S^{2-}, and was not oxidation.

Potentiodynamic tests showed that the CSV3 anode was inactive towards CH_4; in fact, no current withdrawal was possible under either pure methane or pure hydrogen. The cell showed no activity upon heating in H_2, and the ohmic resistance of the cell was high, typically 10 Ω cm^2 or greater. Upon introduction of H_2S fuel the resistance dropped and the activated catalyst was highly active towards H_2S, but remained inactive to H_2 and CH_4. This interpretation is fully consistent with the changes in the impedance spectra (Fig. 6). The polarization resistance, as characterized by the second semicircle (the first semicircle is ascribed to the reaction at the Pt cathode), was increased when in the presence of only N_2 and CH_4, and decreased when H_2S was present, especially at higher concentrations. The anode was active for H_2S electro-oxidation, whether the fuel stream was diluted with either or both of N_2 and CH_4. Each diluent impeded the gas phase diffusion of H_2S to the active sites. Under OCV conditions methane impeded the conversion of H_2S more than N_2, and so the semicircle was larger when methane was the diluent. The cause of this effect may be reversible adsorption of methane at catalyst sites, as shown by the high OCV in the presence of methane, a characteristic of the methane electro-oxidation reaction. However, under polarization conditions the IV curves were similar for each mixed feed of the same H_2S concentration, consistent with conversion of only H_2S. Increasing the H_2S concentration 10-fold led to a 3-fold increase in fuel cell performance, attributed wholly or in large part to a 1 Ω cm^2 decrease in the anode polarization resistance, R_{P2}. These results indicated that the CSV3 anode

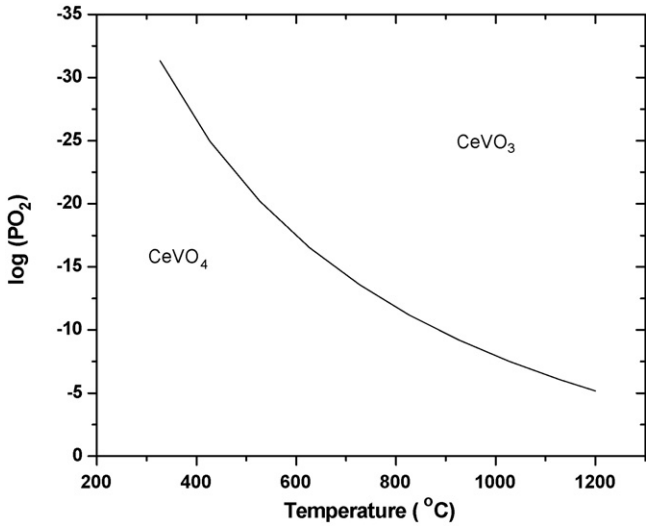

Fig. 12. Thermodynamic stability regions for $CeVO_3$ and $CeVO_4$.

was highly active towards H_2S, similar to the activity for the related oxide anode $La_{0.7}Sr_{0.3}VO_3$ [29–32].

It is noteworthy that the activity of the anode catalyst under thermal catalytic oxidation conditions [35–37] differed from that under the above fuel cell conditions. Whereas the catalyst converted both H_2S and CH_4 in the presence of an atmosphere containing oxygen, the electrochemical process oxidized only H_2S. Thus it appears that conversion of CH_4 requires a significantly elevated concentration of O species at the catalyst surface, and this did not occur under fuel cell operating conditions, especially in the presence of H_2S [45].

The conductivity change resulting from the conversion of the oxide to sulfide was consistent with the low performance of the material in non-H_2S-containing feed gases, and also explained why the performance was so similar at 800 and 950 °C, since the conductivity was higher at the lower temperature. The increase in conductivity was balanced by a decrease in ionic conductivity as well as activation polarization. The stability of CSV3 towards carbon deposition and sulfur poisoning, as opposed to activation as a result of sulfidation, was confirmed by stability of performance during long-term electrochemical tests.

The OCV in all cases was higher than that predicted by the Nernst equation for the pure components, which may be a consequence of changes in the partial pressures of the components of the gas due to secondary reactions occurring in the gas phase while the gas traveled through the heated mullite tube towards the reaction zone [30].

Substitution of a multivalent rare earth cation, $Ce^{3+/4+}$ for La^{3+} in $Ce_{0.9}Sr_{0.1}VO_3$ resulted in an improvement in performance in 5% H_2S–N_2 at 950 °C [30]. The conductivity of CSV3 was similar to that of $LaVO_3$, but only approached that of Sr substituted $LaVO_3$ after the sulfidation reaction [31]. Therefore, the activity of CSV3 can be ascribed to an improvement in activity for H_2S electro-oxidation. It is not clear whether the same transition from oxide to sulfide also occurred in $LaVO_3$, as thermodynamic calculations and stability tests indicated that it is thermally stable in H_2S [32].

The XPS results clearly showed the presence of both oxygen and sulfur species in the sulfided material. Furthermore, a predominant amount of oxygen, relative to sulfur, was present in the near-surface. Analysis of the XPS spectra showed the O/cat ratio decreased slightly after sulfidation, and the ratio of O/cat was four and a half times as large as the S/cat ratio, but that the total surface anion/cation ratio was approximately constant. The nature of the samples and the testing apparatus made it impossible to fully shield the sample from atmosphere after testing. Based on research by Lau and Fang [40], exposure of samples of lanthanum oxide, lanthanum hydroxide and lanthanum oxysulfide to atmosphere did not produce experimentally significant changes in their XPS patterns. Therefore, we expected that any oxygen adsorbed from the atmosphere would be small and would not significantly affect our XPS data.

With sulfidation, a small fraction of Ce^{3+} may have been partly oxidized to Ce^{4+} to accommodate the oxysulfide. However, as the overall anion/cation ratio was unchanged, it is more likely that the shift in positions of XPS peaks was caused by a change in anion species to which Ce cations were neighbours. The peaks for V^{3+} also underwent consequential small shifts after sulfidation, again probably due to bonding of V with sulfur. The V ionic ratios did not appear to change, as indicated by the relative peak areas, indicating that the oxidation state did not change. Therefore, Ce and V both participated in some manner in the sulfidation reaction, which provided a different mechanism from low temperature oxidation of H_2S on $CeVO_4$, where only $Ce^{3+/4+}$ was found to participate in the reaction [46].

For effective, stable operation of a fuel cell, the anode material must be electronically and ionically conductive. CSV3 was used as a single component mixed ionic and electronic conducting catalyst. Thus, during fuel cell testing when the anode underwent the phase transformation from $Ce_{0.9}Sr_{0.1}VO_3 \rightarrow Ce_{0.9}Sr_{0.1}V(O,S)_3$ in a H_2S-containing environment, it must have sustained the reaction by continuing to conduct oxygen ions. In the fuel cell with a potential and chemical gradient in effect across the membrane, conducting oxygen ions from the electrolyte into the anode structure would have kept replenishing the structure with structural oxygen. Thus the anode material in the MEA always included some steady proportion of both oxide and sulfide ions, with the formula $Ce_{0.9}Sr_{0.1}V(O,S)_3$, since the MEA retained its activity for extended periods of time, as found during operation under galvanostatic conditions.

The DSC/TGA results revealed important information regarding what occurred to the anode during fuel cell testing. The initial exothermic peak and final endothermic peaks shown in Fig. 10b were attributed primarily to adsorption and desorption of H_2S on the surface as the materials underwent chemical reactions (3)–(5):

$$H_2S_{(g)} + 2* \rightarrow *HS + *H \rightarrow *S + *2H \quad (3)$$

$$2*H + O^{2-} \rightarrow H_2O_{(g)} + 2e^- \quad (4)$$

$$*S + 2e^- \rightarrow S^{2-} \quad (5)$$

H_2S adsorbed onto the surface dissociated according to reaction (3) to form surface *HS and *H species, and *HS further dissociated to *H and *S species. When surface *H reacted with O^{2-} species, reaction (4), the released electrons then ionized the adsorbed *S according to reaction (5). We propose that the ionized S^{2-} diffused into the structure of $Ce_{0.9}Sr_{0.1}VO_3$, substituted for O^{2-} and so formed $Ce_{0.9}Sr_{0.1}V(O,S)_3$. Once the majority of surface oxygen was removed, the reactants were depleted and the reaction no longer proceeded at the same rate. However, in the electrochemical environment of the fuel cell there was an applied O^{2-} flux that replenished the oxide ion concentration.

Hydrogen sulfide has two possible electrochemical oxidation reactions in fuel cells (6) and (7), and a third oxidation of the product S_2 by reaction (8). Additionally, indirect conversion can be accomplished via two further chemical reactions, a thermal decomposition reaction (9) and a reforming reaction (Claus reaction) (10). The nature of each of these reactions is complex, and involves adsorption, dissociation, electron transfer, bond formation, and desorption steps.

$$H_2S + O^{2-} \rightarrow (1/2)S_2 + H_2O + 2e^-$$

$$OCV(800\,^\circ C/950\,^\circ C) = 0.78\,V/0.78\,V \quad (6)$$

$$H_2S + 3O^{2-} \rightarrow SO_2 + H_2O + 6e^-$$

$$OCV(800\,^\circ C/950\,^\circ C) = 0.75\,V/0.73\,V \quad (7)$$

$$S_2 + 4O^{2-} \rightarrow 2SO_2 + 8e^-$$

$$OCV(800\,^\circ C/950\,^\circ C) = 0.71\,V/0.74\,V \quad (8)$$

$$H_2S \rightarrow S_2 + H_2 \quad (9)$$

$$H_2S + SO_2 \leftrightarrow 3/nS_n + 2H_2O \quad n = 2\text{–}8 \quad (10)$$

H_2S chemisorbs on the surface of the anode where, most likely, it is attracted by the V^{3+} sites. It dissociates to H^+ and S^{2-} which, with electron transfers, electrochemically react with either O^{2-} (transferred from the cathode) or with other S species (from other dissociated H_2S molecules or the sulfided anode) to form the products H_2O, S_2 or SO_2.

One possible means by which the anode operated was that reduced CSV3 was present near the electrolyte, while the rest of the anode was $Ce_{0.9}Sr_{0.1}V(O,S)_3$. The oxide portion provided the

O^{2-} anions for the reactions that occurred on the active layer of the anode which consisted of $Ce_{0.9}Sr_{0.1}V(O,S)_3$ with the actual reaction occurring at triple phase boundaries throughout the anode. As Ferrizz et al. have shown [47], the oxidation state and S content in the Ce–O–S system was dependent on both temperature and partial pressures of both oxygen and sulfur. Thus it was possible to have a gradient of concentrations of oxide and sulfide ions within the structure of the anode under reaction conditions.

A second explanation for the activity of the anode, and more plausible explanation based on the available evidence, is that the structure of a part or all of the anode itself changed from tetragonal to monoclinic with very little sulfur content, while the bulk of the lattice sites were still occupied by oxygen. This, too, would be consistent with the stability of the oxide ion conduction in the fuel cell mode. The DSC/TGA data also supported this hypothesis because the weight of the sample did not continue to increase with exposure to H_2S under non-conductive conditions, meaning that there was no additional uptake of H_2S onto the material, and no migration of sulfide ions into the bulk under DSC/TGA experimental conditions. Furthermore, the XPS data also supported this conclusion, as the amount of bound oxygen in the near-surface was over four times greater than bound sulfur. The XRD data also showed that there were intensity differences for some peaks, which can be explained by O occupying S sites, resulting in a lower intensity due to O scattering, so that it textured the XRD signal. The co-existence of S within oxide structures was found for NiO saturated with S, and for $NiO–Ni_3S_2$ [48]. However, in those situations the presence of sulfide caused a decrease in the conductivity by binding electron holes to the S anions. Furthermore, Lince and Hilton found that O content in the structure of sputtered MOS_2 films was on the order of 10–20 at.%, thus forming $MoS_{2-x}O_x$ which had a significant effect on the tribological properties of that material [49].

While the available evidence does not allow full elucidation of the phenomena occurring in the anode catalyst material during use under electrochemical operations, the evidence makes it clear that the partially sulfided catalyst $Ce_{0.9}Sr_{0.1}V(O,S)_3$ is very effective for conversion of H_2S and does not convert methane or H_2 diluents.

Interestingly, the electrochemical data show no dependence of conductivity of the material (ohmic resistance) on concentration of H_2S. The TG–DSC measurements were made in a 500 ppm H_2S stream. The XPS data were for the material exposed to 5% H_2S. The data correlated well as the S surface coverage was about 15% as determined by TGA and 13% from XPS, essentially similar values despite the difference in H_2S concentrations. Thus the extent of the sulfidation reaction appears to reach a limiting or equilibrium extent at a concentration at or below 500 ppm H_2S.

5. Conclusions

New Ce- and V-containing perovskite and zircon-type oxide anode materials were tested in H_2S- and CH_4-containing atmospheres. We found that:

1. $Ce_{0.9}Sr_{0.1}VO_4$ anodes were reduced in 0.5% $H_2S–CH_4$ and in H_2-containing atmospheres. Due to the dimensional changes associated with the reduction of the oxide when bonded to an electrolyte, this material was not a suitable anode.
2. $Ce_{0.9}Sr_{0.1}VO_3$ anodes are chemically stable in 0.5% $H_2S–CH_4$ at 950 °C for 12 h under non-electrochemical conditions, but $Ce_{0.9}Sr_{0.1}V(O,S)_3$ was formed under 5% H_2S during conductivity measurements, as determined using XRD and XPS analyses.
3. $Ce_{0.9}Sr_{0.1}VO_3$ anodes had high activity only after the introduction of H_2S to the fuel feed. A possible explanation for the sustainable electrochemical activity of sulfided $Ce_{0.9}Sr_{0.1}VO_3$ catalyst, consistent with XPS, XRD and DSC/TGA results, is that the structure of the anode must contain a significant portion of O^{2-} to sustain fuel cell activity, such a structure was denoted as $Ce_{0.9}Sr_{0.1}V(O,S)_3$.
4. After initially forming $Ce_{0.9}Sr_{0.1}V(O,S)_3$ the anodes were only active towards the oxidation of H_2S in the fuel feed. A maximum power density of 140 mW cm^{-2} was achieved at 950 °C in 5% $H_2S–N_2$.

Acknowledgments

This research was supported through funding to the NSERC Solid Oxide Fuel Cell Canada Strategic Research Network from the Natural Science and Engineering Research Council (NSERC). The authors would like to thank S. Merali (XRD), M. Danaie (SEM), D. Karpuzov and A. He (XPS), W. Anh and B. Shalchi (BET) for assistance with characterization equipment.

References

[1] N.Q. Minh, Solid State Ionics 174 (2004) 271–277.
[2] F.Y. Wang, G.B. Jung, A. Su, S.H. Chan, X. Hao, Y.C. Chiang, J. Power Sources 185 (2008) 862–866.
[3] M.R. Pillai, I. Kim, D.M. Bierschenk, S.A. Barnett, J. Power Sources 185 (2008) 1086–1093.
[4] D.D. Burnette, G.G. Kremer, D.J. Bayless, J. Power Sources 182 (2008) 329–333.
[5] X.F. Ye, S.R. Wang, Z.R. Wang, L. Xiong, X.E. Sun, T.L. Wen, J. Power Sources 177 (2008) 419–425.
[6] H. Kishimoto, K. Yamaji, T. Horita, Y.P. Xiong, N. Sakai, M.E. Brito, H. Yokokawa, J. Power Sources 172 (2008) 67–71.
[7] Z.F. Zhou, R. Kumar, S.T. Thakur, L.R. Rudnick, H. Schobert, S.N. Lvov, J. Power Sources 171 (2007) 856–860.
[8] K. Xie, Q.L. Ma, B. Lin, Y.Z. Jiang, J.F. Gao, X.Q. Liu, G.Y. Meng, J. Power Sources 170 (2007) 271–277.
[9] H.P. He, A. Wood, D. Steedman, M. Tilleman, Solid State Ionics 179 (2008) 1478–1482.
[10] K. Haga, S. Adachi, Y. Shiratori, K. Itoh, K. Sasaki, Solid State Ionics 179 (2008) 1427–1431.
[11] Z. Cheng, M. Liu, Solid State Ionics 178 (2007) 925–935.
[12] M. Gong, X. Liu, J. Trembly, C. Johnson, J. Power Sources 168 (2007) 289–298.
[13] C.M. Grgicak, J.B. Giorgi, J. Phys. Chem. C 111 (2007) 15446–15455.
[14] C.M. Grgicak, M.M. Pakulska, J.S. O'Brien, J.B. Giorgi, J. Power Sources 183 (2008) 26–33.
[15] C.M. Grgicak, R.G. Green, J.B. Giorgi, J. Power Sources 179 (2008) 317–328.
[16] V. Vorontsov, J.L. Luo, A.R. Sanger, K.T. Chuang, J. Power Sources 183 (2008) 76–83.
[17] X.J. Chen, Q.L. Liu, S.H. Chan, N.P. Brandon, K.A. Khor, J. Electrochem. Soc. 154 (2007) B1206–B1211.
[18] Z.R. Xu, J.L. Luo, K.T. Chuang, A.R. Sanger, J. Phys. Chem. C 111 (2007) 16679–16685.
[19] J.L. Gadon, Rev. Inst. Fr. Petr. 42 (1987) 685–693.
[20] E.N. Tiratsoo, Oilfields of the World, Gulf Publishing Co., Houston, TX, 1976.
[21] F.N. Cayan, M. Zhi, S.R. Pakalapati, I. Celik, N. Wu, R. Gemmen, J. Power Sources 185 (2008) 595–602.
[22] R. Lohsoontorn, D.J.L. Brett, N.P. Brandon, J. Power Sources 183 (2008) 232–239.
[23] J.P. Trembly, R.S. Gemmen, D.J. Bayless, J. Power Sources 171 (2007) 818–825.
[24] Z. Cheng, M. Liu, J. Electrochem. Soc. 155 (2008) B449–B454.
[25] J.W. Fergus, Solid State Ionics 177 (2006) 1529–1541.
[26] J.B. Goodenough, Y.H. Huang, J. Power Sources 173 (2008) 1–10.
[27] E.V. Tsipis, V.V. Kharton, J.R. Frade, J. Eur. Ceram. Soc. 25 (2005) 2623–2626.
[28] A. Watanabe, J. Solid State Chem. 153 (2000) 174–179.
[29] Z. Cheng, S. Zha, L. Aguilar, D. Wang, J. Winnick, M. Liu, Electrochem. Solid State Lett. 9 (2006) A31–A33.
[30] L. Aguilar, S. Zha, Z. Cheng, J. Winnick, M. Liu, J. Power Sources 135 (2004) 17–24.
[31] Z. Cheng, S. Zha, L. Aguilar, M. Liu, Solid State Ionics 176 (2005) 1921–1928.
[32] Z. Cheng, S. Zha, M. Liu, J. Electrochem. Soc. 153 (2006) A1302–A1309.
[33] C. Sun, U. Stimming, J. Power Sources 171 (2007) 247–260.
[34] C. Reiichi, Y. Bunichi, S. Yoji, T. Yoshitaka, A. Masayasu, Japanese Patent, JP2004186148A.
[35] C.T. Au, W.D. Zhang, H.L. Wan, Catal. Lett. 37 (1996) 241–246.
[36] K.-T. Li, Z.-H. Chi, Appl. Catal. A 206 (2001) 197–203.
[37] M. Bellakki, T. Baidya, C. Shivakumara, N. Vasanthacharya, M. Hegde, G. Madras, Appl. Catal. B 84 (2008) 474–481.
[38] N. Danilovic, V. Alzate-Restrepo, Z.R. Xu, K.T. Chuang, J.M. Hill, J.L. Luo, A.R. Sanger, Appl. Catal. A, in preparation.
[39] C. Kittel, Introduction to Solid State Physics, 8th ed., Wiley, Berkley, CA, 2005.
[40] N.T. Lau, M. Fang, J. Catal. 179 (1998) 343–349.
[41] D. Gonbeau, C. Guimon, G. Pfister-Guillouzo, A. Levasseur, G. Meunier, R. Dormoy, Surf. Sci. 254 (1991) 81–89.
[42] D. Lichtman, J.H. Craig Jr., V. Sailer, M. Drinkwine, Appl. Surf. Sci. 7 (1981) 325–331.

[43] M. Dorogova, A. Navrotsky, L.A. Boatner, J. Solid State Chem. 180 (2007) 847–851.
[44] H. Yokokawa, N. Sakai, T. Kawada, M. Dokiya, Solid State Ionics 52 (1992) 43–56.
[45] M. Mogensen, K. Kammer, Annu. Rev. Mater. Res. 33 (2003) 321–331.
[46] S. Yasyerli, G. Dogu, T. Dogu, Catal. Today 117 (2006) 271–278.
[47] R.M. Ferrizz, R.J. Gorte, J.M. Vohs, Appl. Catal. B 43 (2003) 273–280.
[48] V.B. Tare, J.B. Wagner, J. Appl. Phys. 54 (1983) 252–257.
[49] J.R. Lince, M.R. Hilton, Surf. Coat. Technol. 43/44 (1990) 640–651.